

Observation of a Pressure-Induced Topological Quantum Phase Transition in BiTeI

Xiaoxiang Xi,¹ Chunli Ma,^{2,3} Zhenxian Liu,² Zhiqiang Chen,⁴
Wei Ku,⁵ H. Berger,⁶ C. Martin,⁷ D. B. Tanner,⁷ and G. L. Carr¹

¹*Photon Sciences, Brookhaven National Laboratory, Upton, New York 11973, USA*

²*Geophysical Laboratory, Carnegie Institution of Washington, Washington D.C. 20015, USA*

³*State Key Laboratory of Superhard Materials, Jilin University, Changchun 130012, China*

⁴*Department of Geosciences, Stony Brook University, Stony Brook, New York, USA*

⁵*Condensed Matter Physics and Materials Science Department,
Brookhaven National Laboratory, Upton, New York 11973, USA*

⁶*Institute of Condensed Matter Physics, École Polytechnique Fédérale de Lausanne, CH-1015 Lausanne, Switzerland*

⁷*Department of Physics, University of Florida, Gainesville, Florida 32611, USA*

(Dated: May 7, 2013)

We report the observation of a pressure-induced topological quantum phase transition in the polar semiconductor BiTeI using X-ray powder diffraction and infrared spectroscopy. The X-ray data confirm that BiTeI remains in its ambient-pressure structure up to 8 GPa. The lattice parameter ratio c/a shows a minimum between 2.0–2.9 GPa, indicating an enhanced c-axis bonding through p_z band crossing as expected during the transition. Over the same pressure range, the infrared spectra reveal a maximum Drude spectral weight, reflecting the closing and reopening of the semiconducting gap through band inversion. Both of these features are characteristics of a topological quantum phase transition, and are consistent with a recent theoretical proposal.

PACS numbers: 64.70.Tg, 71.70.Ej, 78.20.-e, 61.05.cp

Topological insulators are a class of materials with an insulating bulk and protected metallic edge or surface states [1]. This intriguing state of matter was theoretically predicted [2–6] and experimentally observed [7–13] in a variety of 2D and 3D systems. In the search for topological insulators, a guiding principle is to identify materials having band inversion at special time-reversal-invariant momentum points of the Brillouin zone, or to induce such a band inversion in suitable systems [1, 3]. This necessary condition was convincingly demonstrated in BiTeI($\text{S}_{1-x}\text{Se}_x$)₂ [14, 15] and (Bi_{1-x}In_x)₂Se₃ [16, 17] by doping, and in bismuth [18] by substrate-induced strain. The effects of doping and strain in these experiments are to tune the spin-orbit interaction and/or the lattice parameters, driving the system through a topological quantum phase transition (TQPT). Such effects can be realized directly by pressure, a method that does not involve the potential defects and inhomogeneity of doping and offers more tunability than substrate-induced strain. This has indeed been proposed as a means to look for a topological insulating state in, e.g., ternary Heusler compounds [19], $\text{A}_3\text{Ir}_2\text{O}_7$ ($\text{A} = \text{Y}$ or rare-earth elements) [20], $\text{Ge}_2\text{Sb}_2\text{Te}_5$ [21], and BiTeI [22]. Despite its importance to the field, there has been no experimental indication for a pressure-tuned topological insulator.

The prediction of pressure-induced TQPT in BiTeI is particularly interesting [22]. BiTeI is a layered polar semiconductor with the trigonal space group $P3m1$ and a hexagonal unit cell at ambient pressure [23]. The triple Te-Bi-I layers stack along the crystallographic c axis, coupled by the Van der Waals interaction. The broken inversion symmetry in the presence of strong spin-orbit coupling gives rise to a giant Rashba-type spin splitting,

the largest observed so far in any system [24]. Although BiTeI is a narrow-gap semiconductor with an ambient-pressure band gap of ~ 0.38 eV [24–26], it is typically self-doped due to non-stoichiometry and thus an n-type semiconductor [27]. Remarkably, Bahramy *et al.* [22] predicted that hydrostatic pressure effectively tunes the crystal-field splitting and spin-orbit interaction in BiTeI, turning it into a topological insulator. Such a TQPT is accompanied by a band inversion near the A point of the Brillouin zone; the dispersion of the bulk spin-split bands becomes almost linear at the critical pressure P_c .

In this Letter, we report experimental observation of characteristics of such a pressure-induced TQPT in BiTeI using X-ray powder diffraction and infrared spectroscopy. X-ray powder diffraction shows that BiTeI remains in the hexagonal structure up to 8 GPa but with the lattice parameter ratio c/a passing through a minimum between 2.0 and 2.9 GPa, indicating an enhanced c-axis bonding through p_z band crossing. Infrared spectroscopy over the same pressure range reveals a maximum in the free carrier spectral weight as would be expected when the semiconducting band gap closes and reopens through band inversion. Both of these results provide evidence for a pressure-induced TQPT in BiTeI at a critical pressure P_c between 2.0 and 2.9 GPa [22]. Our experiments demonstrate pressure as an efficient way to induce TQPTs and the use of infrared spectroscopy and X-ray diffraction for their investigation.

Single crystals of BiTeI were grown by the Bridgman method. The ambient-pressure carrier density is estimated to be $2.7 \times 10^{19} \text{ cm}^{-3}$ [28]. Samples used in different experiments were mechanically cleaved from one single crystal. High-pressure infrared spectroscopy and

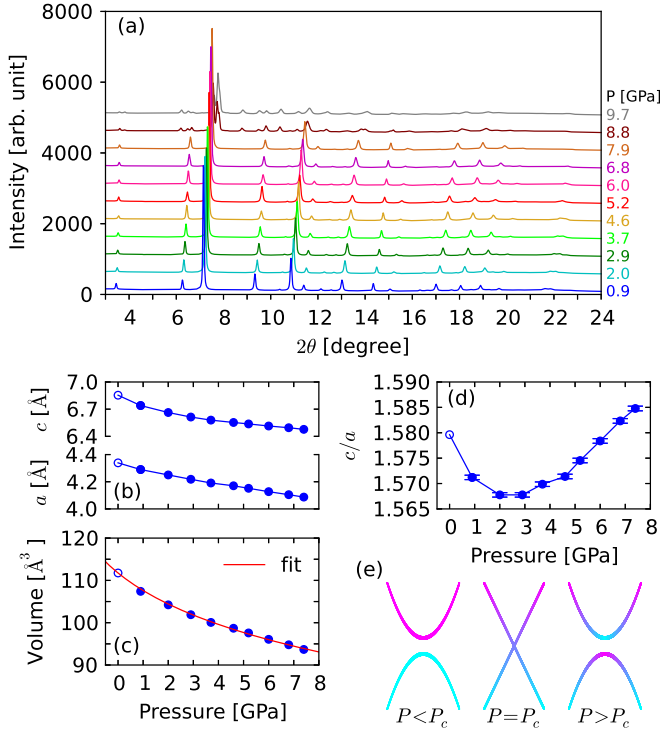


FIG. 1. (color online). (a) X-ray powder diffraction patterns of BiTeI from 0.9 to 9.7 GPa. The data above 0.9 GPa are vertically shifted for clarity. The filled circles in (b), (c), and (d) are the lattice parameters c and a , the unit-cell volume, and the c/a ratio in the hexagonal phase at different pressures, extracted from our XRD data. The open circles are the ambient-pressure data taken from Ref [23]. The solid line in (c) is a fit to a Birch-Murnaghan equation of state. The error bars in (d) come from the uncertainties in c and a . (e) A diagram illustrates the band inversion across the TQPT at P_c . Magenta denotes the Bi-6 p_z orbital; cyan denotes the Te-5 p_z and I-5 p_z orbitals.

angle-dispersive X-ray powder diffraction were performed at U2A and X17C beamlines at the National Synchrotron Light Source (Brookhaven National Laboratory). All data were collected at room temperature. Pressure was monitored by laser-excited ruby fluorescence. The separation of the two fluorescence lines indicated that the pressure was quasi-hydrostatic. In the X-ray diffraction (XRD) experiment, a sample was ground into fine powder and loaded into a diamond anvil cell (DAC). A 4:1 methanol-ethanol mixture was used as the pressure-transmitting medium. Two-dimensional diffraction rings were collected for pressures up to 27.2 GPa, with the incident monochromatic X-ray wavelength set to 0.4066 Å. Integrating the diffraction rings yielded XRD patterns as a function of the diffraction angle 2θ [29].

The experimental configuration for the infrared measurements is illustrated in the inset of Fig. 2b. The sample was pressed against a diamond anvil and surrounded by a pressure-transmitting medium (KBr) elsewhere. In-

frared microspectroscopy was performed on an FT-IR spectrometer coupled to a microscope [30]. Near-normal incidence reflectance and transmittance were measured for photon energies between 0.08–1.00 eV and pressures up to 25.2 GPa. Four samples were measured, all giving consistent results. The data with the most complete pressure dependence are presented here.

The XRD patterns in Fig. 1a show a structural phase transition at ~ 8 GPa. Ambient-pressure BiTeI has a hexagonal lattice with lattice parameters $a = 4.339$ Å and $c = 6.854$ Å [23]. Increasing pressure consistently shifts each Bragg peak to a larger 2θ angle, indicating the reduction of the d -spacing. Above 7.9 GPa, a great number of new peaks emerge, suggesting a different structure. We analyzed the XRD patterns [31] and discuss here the results for the hexagonal phase. The analysis yields the lattice parameters (Fig. 1b) and the unit-cell volume (Fig. 1c). We include the ambient-pressure values of these parameters taken from Ref [23] (omitted in our experiment), shown as open circles in Fig. 1b,c; they are consistent with the pressure dependence of our data. A least-square fit of the unit-cell volume to a Birch-Murnaghan equation of state [32] yields the bulk modulus $B_0 = 23.1$ GPa and its pressure derivative $B'_0 = 7.2$.

The ratio c/a shown in Fig. 1d has a clear minimum between 2.0–2.9 GPa, strongly indicating a change in the chemical bonding across the TQPT. In a topologically-trivial insulator, a TQPT occurs when the atomic orbital energy ordering near the Fermi level reverses and the conduction (valence) band inverts. The diagram in Fig. 1e illustrates this process. In ambient-pressure BiTeI, the bottom conduction bands are dominated by the Bi-6 p_z orbital while the top valence bands are dominated by the Te-5 p_z (and I-5 p_z) orbital [22, 33]; that is, within the low-energy bands, the bonding is almost ionic in nature for $P < P_c$. After the pressure-induced band inversion happens ($P > P_c$), one expects the Te-5 p_z orbital contributes to the bottom conduction bands and the Bi-6 p_z orbital dominates the top valence bands; the bonding becomes more covalent. At the transition ($P = P_c$), additional metallic bonding occurs involving the p_z orbitals of Bi and Te, whose charge fluctuation would make the c -axis more compressible. This is observed clearly as a minimum in the ratio c/a , which indicates a TQPT at P_c between 2.0–2.9 GPa. The corresponding volume contraction is 7–9%, similar to the theoretically predicted 11% [22]. Thus, we have the first piece of strong evidence of a TQPT.

Next, infrared spectroscopy reveals more detailed information on the electronic structure in this pressure range and indicates a TQPT as well. In the hexagonal phase, the reflectance (Fig. 2a) shows a plasma edge characteristic of the free carrier response in the system. In 0–2.20 GPa, the plasma edge gradually blue shifts upon pressure increase. Above 2.20 GPa, it plunges to a lower photon energy and keeps red shifting when the pressure

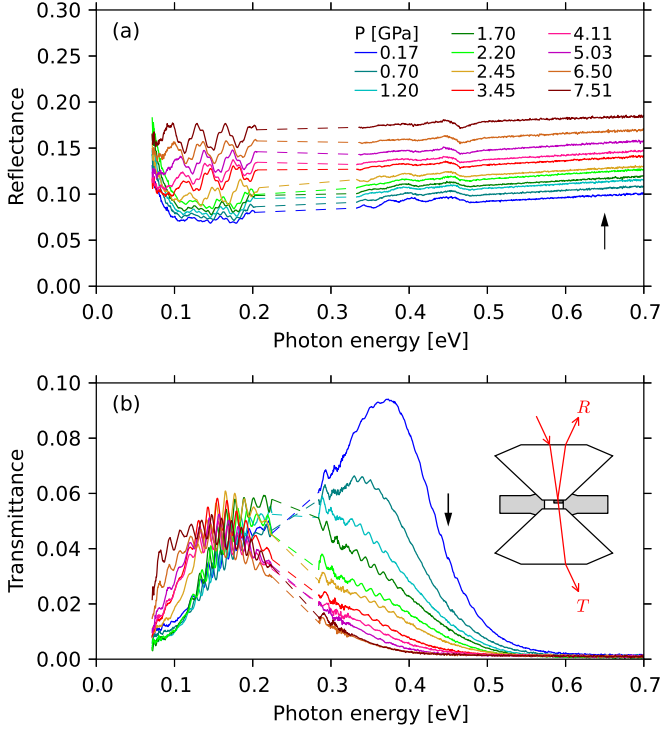


FIG. 2. (color online). Infrared reflectance (a) and transmittance (b) of BiTeI for pressure in 0.17–7.51 GPa. The arrows indicate the direction of increasing pressure. Absorption from diamond corrupts the data between 0.22–0.33 eV (patched as dashed lines) and causes the dip at ~ 0.46 eV in reflectance. The inset in (b) shows the measurement configuration. The arrowed lines indicate the beam paths for the reflected (R) and transmitted (T) signals.

is further increased. The transmittance (Fig. 2b) also shows dramatic pressure dependence. Between 0.08–0.20 eV, it changes slowly below 2.20 GPa but jumps to a higher level at 2.45 GPa, indicating a reduction of absorption. Both the reflectance and the transmittance contain fringes; they arise because of the Fabry-Pérot effects in the optically-flat sample and in the KBr. The thinner sample gives rise to the broad fringes and the thicker KBr gives rise to the fine ones [30]. When pressure is increased above 2.20 GPa, the contrast of the broad fringes in reflectance improves significantly. This suggests a sudden reduction of absorption right above 2.20 GPa at the photon energies where the broad fringes reside, corroborating the aforementioned sudden increase in transmittance. Evidently a transition happens in the 2.20–2.45 GPa range, coinciding with the pressure where the minimum c/a occurs. We note that the turning of the plasma edge at ~ 2 GPa was consistently observed in the four samples we measured, although the quantitative behavior of the infrared data is sample dependent on account of differing scattering rates in the samples. For the discussion that follows and to simplify the analysis, we remove the fringes by Fourier transforming the data and

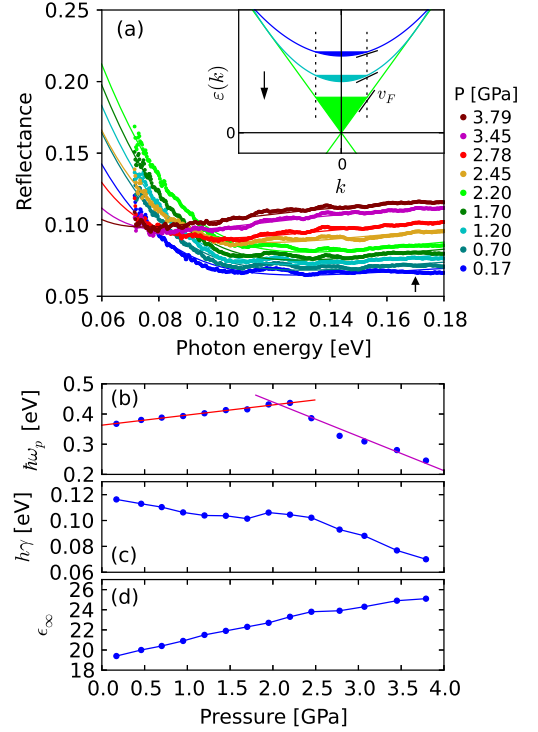


FIG. 3. (color online). (a) Reflectance at low pressure and low photon energy, after fringe removal. The solid lines are fits to the Drude model. The inset illustrates the conduction band dispersion $\varepsilon(k)$ and the chemical potential as the pressure approaches P_c . The slope of $\varepsilon(k)$ at the chemical potential gives the Fermi velocity v_F . The arrows indicate the direction of increasing pressure. (b–d) Pressure dependence of the fitting parameters for the Drude model, i.e. the plasma frequency ω_p , the electronic scattering rate γ , and the dielectric constant ϵ_∞ due to high-energy incoherent excitations. The solid lines in (b) are linear fits to the parts before and after the maximum.

filtering the fringe signatures.

We adopt the following approach to analyze the infrared spectra after fringe removal. The sample and the pressure-transmitting medium are considered as a double-layer slab sandwiched between the diamond anvils. Incoherently adding intensities of multiple internal reflections in the double layers gives the reflectance and transmittance [30]. The equations involve the sample thickness, which was obtained by estimating its ambient-pressure value and using the pressure dependence of c determined from XRD [30].

Below 0.2 eV, the free carrier absorption dominates. The Drude model adequately describes the free carrier response, with a dielectric function

$$\epsilon = \epsilon_\infty - \frac{\omega_p^2}{\omega^2 + i\omega\gamma}. \quad (1)$$

Here ϵ_∞ is the dielectric constant contributed from high-energy incoherent excitations, ω_p the plasma frequency, and γ the electronic scattering rate. A least-square fit to

Eq. (S1) in [30] was performed on reflectance, shown as solid lines in Fig. 3a. The fitting parameters are shown in Fig. 3b,c,d. The plasma frequency at the lowest pressure is $5.59 \times 10^{14} \text{ s}^{-1}$, close to the ambient-pressure value obtained from an infrared measurement performed on the same sample [26]. Using the effective mass $m^* = 0.19m_0$ (m_0 is the electron mass) [28], we estimate the free carrier density $n = 1.9 \times 10^{19} \text{ cm}^{-3}$ from $\omega_p = \sqrt{4\pi n e^2 / m^*}$, reasonably consistent with that estimated from quantum oscillation measurements [28]. Compared to an earlier ambient-pressure measurement [26], the scattering rate γ is bigger in the sample studied here, and varies among all the samples measured. The monotonic increase in ϵ_∞ upon pressurization accords with that in reflectance at photon energies greater than 0.3 eV.

The peak at 2.20 GPa in the pressure-dependent ω_p shown in Fig. 3b is a second piece of evidence for the TQPT. Across the TQPT in an insulator, the band gap closes and reopens. Near the band touching point, the dispersion of the conduction and valence bands becomes nearly linear. A simplified picture is illustrated in the inset of Fig. 3a. If electrons occupy the conduction band, the change of the conduction-band dispersion causes a change of the Fermi velocity v_F . This manifests as a change of the Drude spectral weight $\omega_p^2/8$ originating from the carriers lying close to the chemical potential. As illustrated in the inset of Fig. 3a, v_F increases as $P \rightarrow P_c$ (and decreases above P_c when the dispersion again becomes parabolic, not shown). The maximum v_F lies in the transition region where the band dispersion approaches linear behavior, yielding the maximum ω_p around the transition because $\omega_p^2 \propto v_F^2$ [25]. Moreover, v_F is expected to be linear in pressure to the lowest order [34], resulting in the linear dependence of $\omega_p(P)$ before and after the transition, shown as solid lines in Fig. 3b. Thus the observed maximum in the Drude spectral weight clearly indicates the closing and reopening of the semiconducting gap in our naturally doped sample during a TQPT; the critical pressure is consistent with the range given by the X-ray powder diffraction.

We confirm our analysis by the optical conductivity. Using Eqs. (S1) and (S2) in [30], we iteratively solve for the sample refractive index and extinction coefficient. These are used to calculate the optical conductivity; its real part is shown in Fig. 4. The data may be quantitatively inaccurate because of the analysis invoked to account for the complicated measurement configuration, but they show the intraband and interband transitions reported previously in the 0.1–0.6 eV range [25, 26] and hence should be qualitatively correct. The dc conductivity σ_0 , roughly estimated by extrapolating the Drude conductivity to zero photon energy, peaks at 2.20 GPa, consistent with the maximum in $\sigma_0 = \omega_p^2/4\pi\gamma$ calculated using the ω_p and γ from the Drude fit (inset in Fig. 4). The sudden drop of the Drude conductivity above 2.20 GPa results in the fringe contrast improve-

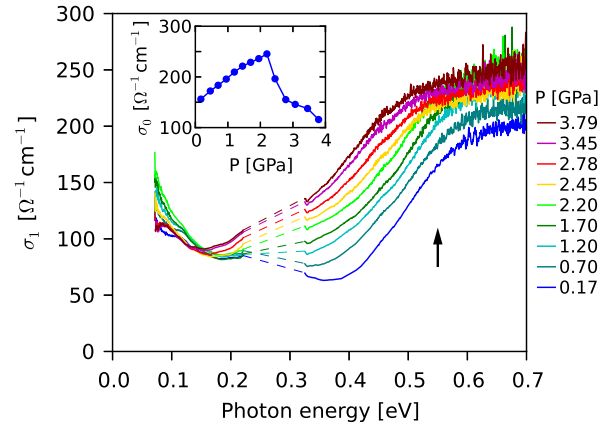


FIG. 4. (color online). The real part of the optical conductivity calculated from reflectance and transmittance. The arrow indicates the direction of increasing pressure. The data between 0.22–0.33 are corrupted by the diamond absorption (patched as dashed lines). The inset shows the dc conductivity σ_0 calculated from ω_p and γ shown in Fig. 3b,c.

ment in reflectance and the increase in transmittance shown in Fig. 2. The band gap closing and reopening associated with the TQPT is not discernible as interband features. This could be accounted for by the self-doping in our sample: the band gap change is severely masked by the Pauli blocking effects because free carriers occupy the conduction band. Measurements on BiTeI samples with intrinsic semiconducting properties, such as that reported in Ref [27], will provide more useful information of the band gap.

In summary, we obtained independent and consistent experimental evidence for a pressure-induced topological quantum phase transition in BiTeI using X-ray powder diffraction and infrared spectroscopy. Across the transition: (i) The lattice parameter ratio c/a shows a minimum; (ii) The Drude spectral weight peaks. Both of these features are characteristics of the topological quantum phase transition, and are consistent with a recent theoretical proposal. Our work motivates the exploration of the novel physics associated with this transition [35] using other experimental probes.

We thank M. S. Bahramy, B.-J. Yang (RIKEN), and Jianming Bai (BNL) for useful discussions. This work was supported by the U. S. Department of Energy through contract DE-AC02-98CH10886 at BNL. The use of U2A and X17C beamline was supported by NSF (DMR-0805056; EAR 06-49658, COMPRES) and DOE/NNSA (DE-FC03-03N00144, CDAC).

-
- [1] M. Z. Hasan and C. L. Kane, Rev. Mod. Phys. **82**, 3045 (2010).
 - [2] B. A. Bernevig, T. A. Hughes, and S. C. Zhang, Science

- 314**, 1757 (2006).
- [3] L. Fu and C. L. Kane, *Phys. Rev. B* **76** 045302 (2007).
 - [4] H. Zhang, C. X. Liu, X. L. Qi, X. Dai, Z. Fang, and S. C. Zhang, *Nat. Phys.* **5**, 438 (2009).
 - [5] B. Yan, C. X. Liu, H. J. Zhang, C. Y. Yam, X. L. Qi, T. Frauenheim, and S. C. Zhang, *Europhys. Lett.* **90**, 37002 (2010).
 - [6] H. Lin, R. S. Markiewicz, L. A. Wray, L. Fu, M. Z. Hasan, and A. Bansil, *Phys. Rev. Lett.* **105**, 036404 (2010).
 - [7] M. König, S. Wiedmann, C. Brüne, A. Roth, H. Buhmann, L. W. Molenkamp, X. L. Qi, and S. C. Zhang, *Science* **318**, 766 (2007).
 - [8] D. Hsieh, D. Qian, L. Wray, Y. Xia, Y. S. Hor, R. J. Cava, and M. Z. Hasan, *Nature* **452**, 970 (2008).
 - [9] D. Hsieh, Y. Xia, L. Wray, D. Qian, A. Pal, J. H. Dil, J. Osterwalder, F. Meier, G. Bihlmayer, C. L. Kane, Y. S. Hor, R. J. Cava, and M. Z. Hasan, *Science* **329** 919 (2009).
 - [10] Y. Xia, D. Qian, D. Hsieh, L. Wray, A. Pal, H. Lin, A. Bansil, D. Grauer, Y. S. Hor, R. J. Cava, and M. Z. Hasan, *Nat. Phys.* **5**, 398 (2009).
 - [11] Y. L. Chen, J. G. Analytis, J. H. Chu, Z. K. Liu, S.-K. Mo, X. L. Qi, H. J. Zhang, D. H. Lu, X. Dai, Z. Fang, S. C. Zhang, I. R. Fisher, Z. Hussain, and Z.-X. Shen, *Science* **325**, 178 (2009).
 - [12] Y. L. Chen, Z. K. Liu, J. G. Analytis, J.-H. Chu, H. J. Zhang, B. H. Yan, S.-K. Mo, R. G. Moore, D. H. Lu, I. R. Fisher, S. C. Zhang, Z. Hussain, and Z.-X. Shen, *Phys. Rev. Lett.* **105**, 266401 (2010).
 - [13] C. Brüne, C. X. Liu, E. G. Novik, E. M. Hankiewicz, H. Buhmann, Y. L. Chen, X. L. Qi, Z. X. Shen, S. C. Zhang, and L. W. Molenkamp, *Phys. Rev. Lett.* **106**, 126803 (2011).
 - [14] S.-Y. Xu, Y. Xia, L. A. Wray, S. Jia, F. Meier, J. H. Dil, J. Osterwalder, B. Slomski, A. Bansil, H. Lin, R. J. Cava, and M. Z. Hasan, *Science* **332**, 560 (2011).
 - [15] T. Sato, K. Segawa, K. Kosaka, S. Souma, K. Nakayama, K. Eto, T. Minami, Y. Ando, and T. Takahashi, *Nat. Phys.* **7**, 840 (2011).
 - [16] M. Brahlek, N. Bansal, N. Koirala, S.-Y. Xu, M. Neupane, C. Liu, M. Z. Hasan, and S. Oh, *Phys. Rev. Lett.* **109**, 186403 (2012).
 - [17] L. Wu, R. V. Aguilar, M. Brahlek, A. V. Stier, Y. Lubashevsky, C. M. Morris, L. S. Bilbro, N. Bansal, S. Oh, and N. P. Armitage, *arXiv:1209.3290*.
 - [18] T. Hirahara, N. Fukui, T. Shirasawa, M. Yamada, M. Aitani, H. Miyazaki, M. Matsunami, S. Kimura, T. Takahashi, S. Hasegawa, and K. Kobayashi, *Phys. Rev. Lett.* **109**, 227401 (2012).
 - [19] S. Chadov, X. L. Qi, J. Kübler, G. H. Fecher, C. Felser, and S. C. Zhang, *Nat. Mat.* **9**, 541 (2010).
 - [20] B.-J. Yang and Y. B. Kim, *Phys. Rev. B* **82**, 085111 (2010).
 - [21] B. Sa, J. Zhou, Z. Song, Z. Sun, and R. Ahuja, *Phys. Rev. B* **84**, 085130 (2011).
 - [22] M. S. Bahramy, B.-J. Yang, R. Arita, and N. Nagaosa, *Nat. Commun.* **3**, 679 (2011).
 - [23] A. V. Shevelkov, E. V. Dikarev, R. V. Shpanchenko, and B. A. Popovkin, *J. Solid State Chem.* **114**, 397 (1995).
 - [24] K. Ishizaka, M. S. Bahramy, H. Murakawa, M. Sakano, T. Shimojima, T. Sonobe, K. Koizumi, S. Shin, H. Miyahara, A. Kimura, K. Miyamoto, T. Okuda, *Nat. Mat.* **10**, 521 (2011).
 - [25] J. S. Lee, G. A. H. Schober, M. S. Bahramy, H. Murakawa, Y. Onose, R. Arita, N. Nagaosa, and Y. Tokura, *Phys. Rev. Lett.* **107**, 117401 (2011).
 - [26] C. Martin, K. H. Miller, S. Buvaev, H. Berger, X. S. Xu, A. F. Hebard, D. B. Tanner, *arXiv:1209.1656*.
 - [27] M. Kanou and T. Sasagawa, *J. Phys.: Condens. Matter* **25** 135801 (2013).
 - [28] C. Martin, E. D. Mun, H. Berger, V. S. Zapf, and D. B. Tanner, *Phys. Rev. B* **87**, 041104(R) (2013).
 - [29] A. P. Hammersley, S. O. Svensson, M. Hanfland, A. N. Fitch, and D. Häusermann, *High Pressure Res.* **14**, 235 (1996).
 - [30] See the details of the infrared measurements, the reflectance and transmittance formula, and the estimation of the sample thickness in the Supplemental Material.
 - [31] A. C. Larson and R. B. Von Dreele, Los Alamos National Laboratory Report LAUR, 86-748 (2000).
 - [32] F. J. Birch, *J. Appl. Phys.* **9**, 279 (1938).
 - [33] M. S. Bahramy, R. Arita, and N. Nagaosa, *Phys. Rev. B* **84**, 041202 (2011).
 - [34] Expanding the pressure-dependent Fermi velocity $v_F(P)$ around P_c , one obtains $v_F(P) = v_F(P_c) + (\partial v_F / \partial P)|_{P_c} \cdot \Delta P + \mathcal{O}(\Delta P^2)$, where $\Delta P = P - P_c$.
 - [35] B.-J. Yang, M. S. Bahramy, R. Arita, H. Isobe, E.-G. Moon, and N. Nagaosa, *Phys. Rev. Lett.* **110**, 086402 (2013).

Supplemental Material

1. Infrared microspectroscopy in a diamond anvil cell

A diamond anvil cell (DAC) with type IIa diamond anvils was used in the infrared microspectroscopy. Infrared spectra were collected on a Bruker Vertex 80v FT-IR spectrometer coupled to a Hyperion 2000 microscope, using a Globar source and an MCT detector. The measurement configuration is shown in Fig. S1. The sample was pressed against the top diamond anvil and surrounded by a pressure-transmitting medium (KBr) elsewhere. The sample covered approximately half of the 300 μm diameter sample chamber in a stainless steel gasket. BiTeI is soft; when compressed in a DAC, it forms a shiny flat surface with the top diamond anvil to make specular reflections. At a given pressure, we first obtained the transmittance: the infrared beam was focused on the KBr next to the sample to collect a reference transmission spectrum T_r , and then on the sample to collect the sample transmission spectrum T_s ; the ratio T_s/T_r gave the sample transmittance. We next obtained the reflectance: the infrared beam was first focused on the sample to collect the sample reflection spectrum R_s , and then on the top diamond-air interface to collect a reference reflection spectrum R_r , yielding a ratio $R_1 = R_s/R_r$. When all the pressure-dependent measurements were finished, we opened the DAC and took the top diamond anvil, which had been in contact with the sample. After cleaning its culet, we measured the reflection spectrum from the top diamond-air interface (R_r) and from the culet-air interface through the anvil (R_c) to yield another ratio $R_2 = R_c/R_r$. The sample reflectance at the sample-diamond interface was calculated as $R_1/R_2 \cdot R_d = R_s/R_c \cdot R_d$, where R_d is the known single-bounce reflectance of diamond at the diamond-air interface. Such a measurement scheme minimized possible systematic errors and the effects due to the absorption from diamond.

The spectra contain broad fringes due to the Fabry-Pérot effects in the sample and fine fringes due to the same effects in the pressure-transmitting medium KBr. Because of our measurement scheme, both broad and fine fringes are present in the reflectance, but only fine fringes dominate in the transmittance. For reflectance, the sample spectrum R_s contains the Fabry-Pérot effects from both the sample and KBr, but the spectra R_r and R_c do not have fringes. The ratio R_s/R_c therefore preserves both the broad and the fine fringes. Because the sample is absorbing, and because the beam has to traverse the sample twice to make the Fabry-Pérot effects in KBr observable in the measured reflectance, the corresponding fringe contrast is weak. Therefore these fine fringes are seen as small oscillations superimposed on a background

of the much broader sample fringes. For transmittance, the reference spectrum T_r was taken in the region next to the sample, where KBr is thicker than that underneath the sample by an amount equal to the sample thickness. This thickness mismatch gives rise to the dominant fine fringes in the transmittance.

2. Reflectance and transmittance of a double-layer slab

The measured reflectance and transmittance can be analyzed by considering the sample (denoted as s) and the pressure-transmitting medium (denoted as m) as a double-layer slab, shown in Fig. S1. This slab is bounded by the diamond anvils (denoted as d) on both sides. Since the fringes were removed from the spectra to simplify the analysis, one can add intensities rather than amplitudes from the multiple internal reflections in s and m . Because the reflectance and transmittance of a single-layer slab is straightforward to obtain, we solve the double-layer slab problem following a two-step method [1]. (i) Solve the single-layer-slab problem, where the slab is m , bounded by s and the bottom d . This gives the reflectance R_{s-md} and transmittance $T_{s-md} = 1 - R_{s-md}$ of a composite medium (denoted as md) consisting of m and the bottom d , interfaced with s . (ii) Solve the single-layer-slab problem, where the slab is s , bounded by the top d and the composite medium md . The reflectance and transmittance for the double-layer slab are

$$R = R_{sd} + \frac{(1 - R_{sd})^2 R_{s-md} e^{-8\pi\kappa\nu x}}{1 - R_{sd} R_{s-md} e^{-8\pi\kappa\nu x}}, \quad (\text{S1})$$

$$T = \frac{(1 - R_{sd})(1 - R_{s-md}) e^{-4\pi\kappa\nu x}}{1 - R_{sd} R_{s-md} e^{-8\pi\kappa\nu x}}, \quad (\text{S2})$$

in which

$$R_{s-md} = R_{sm} + \frac{(1 - R_{sm})^2 R_{md}}{1 - R_{sm} R_{md}}. \quad (\text{S3})$$

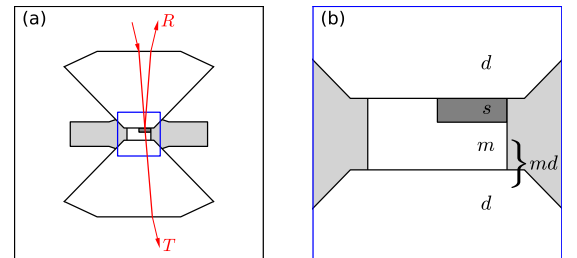


FIG. S1. (a) Measurement configuration for infrared microspectroscopy in a diamond anvil cell. The arrowed lines indicate the beam paths for the reflected (R) and transmitted (T) signals. (b) Close-up of the part in the square in (a). d : diamond anvil. s : sample. m : pressure-transmitting medium. md : composite medium consisting of m and d .

In Eqs. (S1), (S2), and (S3), $R_{sd} = [(n - n_d)^2 + \kappa^2]/[(n + n_d)^2 + \kappa^2]$, $R_{sm} = [(n - n_m)^2 + \kappa^2]/[(n + n_m)^2 + \kappa^2]$, and $R_{md} = (n_m - n_d)^2/(n_m + n_d)^2$ are the single-bounce reflectance at the s - d , s - m , and m - d interfaces, respectively. They involve the to-be-solved sample refractive index n and extinction coefficient κ , and the known refractive index of diamond n_d [2] and KBr n_m [3]. ν is the wavenumber (defined as $1/\text{wavelength}$ with the unit cm^{-1}), and x is the sample thickness. The determination of x is discussed in the next section.

3. Sample thickness

The thickness of the sample in the DAC can be determined from the fringes in the reflectance spectra. We Fourier transformed the raw reflectance spectrum at 0.17 GPa and filtered out the fringe signature due to KBr. This makes the broad fringes due to the sample easier to identify. The broad fringes have a period of $\Delta\nu \approx 300 \text{ cm}^{-1}$. Taking the refractive index of the sample calculated from the Drude fit at this pressure in this photon energy range, $n \approx 4.1$, we determined the sample thickness $x = 1/2n\Delta\nu \approx 4.1 \text{ }\mu\text{m}$. Note that the sample refractive index n is not a known quantity. We initially fitted the reflectance to the Drude model using the single-bounce reflectance formula for the diamond-sample interface, $R_{sd} = [(n - n_d)^2 + \kappa^2]/[(n + n_d)^2 + \kappa^2]$. The refractive index n derived from the fit was used to calculate the sample thickness. The Drude fit was then refined using

Eq. (S1). We checked the resulting n and repeated these procedures, until a self-consistent solution was found. To determine the sample thickness at other pressures, one can use the same procedures described above, or use the pressure dependence of the lattice parameter c obtained from X-ray powder diffraction. The latter approach was adopted in our analysis because it is simpler and probably more accurate compared to the former.

To confirm the validity of the thickness estimation based on fringes, we applied this method to determine the thickness of the pressure-transmitting medium KBr. We obtained the fine-fringe period from the raw transmittance spectrum at 0.17 GPa, $\Delta\nu \approx 83 \text{ cm}^{-1}$. The refractive index of KBr is about 1.53 in the photon energy range where the fine fringes reside. Therefore the substrate thickness is roughly $1/(2 \times 1.53 \times 83 \text{ cm}^{-1}) = 39 \text{ }\mu\text{m}$. Note that we measured the thickness of the stainless-steel gasket to be $\sim 41 \text{ }\mu\text{m}$ before we compressed it between the diamond anvils. This is reasonably close to the estimated KBr thickness.

-
- [1] O. S. Heavens, *Optical Properties of Thin Solid Films* (Dover Publications, New York, 2011).
 - [2] D. F. Edwards and E. Ochoa, J. Opt. Soc. Am. **71**, 607 (1981).
 - [3] R. E. Stephens, E. K. Plyler, W. S. Rodney, and R. J. Spindler, J. Opt. Soc. Am. **43**, 110 (1953).